

Hydrodynamics study on a traveling wave-based undulating surface of a hydrofoil in a free-stream flow

Sarvesh Shukla , Namshad Thekkethil , Atul Sharma ,
Amit Agrawal , and Rajneesh Bhardwaj *

Department of Mechanical Engineering, Indian Institute of Technology Bombay, Mumbai, India 400076



(Received 23 April 2022; accepted 10 August 2022; published 30 August 2022)

A fluid-structure interaction study on free-stream flow across a NACA0012 hydrofoil, with a traveling wave-based surface undulation, is numerically studied at a constant wave number $K = 10$ of the traveling wave and phase difference of 180° between the top and bottom surface undulations. Effect of phase speed c^* (1–10) of the wave, local amplitude-thickness ratio A_L (0.05–0.25), and Reynolds number Re on the near-wake flow characteristics and propulsive performance are investigated. For the various values of the nondimensional governing parameters, the present results revealed two types of vortex patterns: an almost steady vortex sheet and periodic vortex street. Further, forward and reverse types of both vortex sheets and vortex streets are found behind the hydrofoil. A novel two-pair of reverse vortex streets and reverse vortex sheets are found at larger values of c^* , A_L , and Re . Surface undulations cause a high-pressure and high-velocity zone near the troughs of the wave. Consequently, a pressure-suction mechanism in the leeward and forward side of each wavy section produces a spatially varying thrust. The spatial variation of the thrust is attributed to the variation of wave amplitude along the foil. A threshold value of c^* , Re , and A_L exists to produce thrust. A scaling analysis is presented with a power-law scaling for the mean thrust coefficient (C_T) as a function of K , c^* , A_L , with 3, 2, and 3 as the respective exponents. The proposed scaling is found to be consistent with the computations. The present biomimetic fish-inspired study can lead to design and development of a need-based autonomous underwater vehicle or energy harvesting device.

DOI: [10.1103/PhysRevFluids.7.084703](https://doi.org/10.1103/PhysRevFluids.7.084703)

I. INTRODUCTION

Understanding fish locomotion is potentially helpful in designing underwater vehicles for naval applications. With the help of their body, muscles, and appendages, fish manipulate the surrounding hydrodynamics along with an efficient unsteady fluid-structure interaction for efficient propulsion. These manipulations have been done both actively and passively, as described by Fish and Lauder [1]. The classification of passive and active flow control is based on whether an energy input is required or not [2].

Motivated by biolocomotion strategies, previous studies have used these techniques to reduce drag or generate thrust on immersed bodies. *Passive* flow control includes reconfiguration or streamlining of the body due to flexibility of the body [3] or attaching a splitter plate in the downstream of the cylinder to reduce the drag force [4–6]. The shark surfaces have riblets aligned in the direction of fluid flow, which has a reducing drag effect which is generally known as the shark-skin effect [7]. Lee and Nguyen [8] in their experimental study of a wavy cylinder with a

*rajneesh.bhardwaj@iitb.ac.in

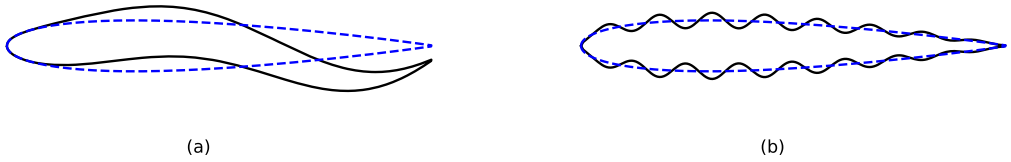


FIG. 1. Schematic for two different types of traveling wave motions that leads to (a) whole body undulation and (b) surface undulation for a NACA0012 hydrofoil. The wave numbers $k = 1$ for (a) and $k = 10$ for (b). The blue dotted profile shows the undeformed hydrofoil.

sinusoidal varying cross-sectional area in a spanwise direction found a significant reduction in drag because of the wavy surface in comparison with a smooth cylinder case.

On the other hand, *active* flow control mechanisms are governed by some energy input causing the movement of the body and its appendages, namely, pitching [9–12], heaving [13–16], undulation motion [17,18], and flapping motion (combined pitching and heaving motions) [19–25]. In general, fish use undulation motion on their body for propulsion, which is a traveling wave on their spinal length with increasing amplitude from head to tail [26,27]. For pure pitching, the optimal thrust for an oscillating hydrofoil is produced for a specific range of Strouhal numbers, i.e., 0.25 to 0.35 [20].

Previous studies reported streamwise traveling wave-based motions of two types: First, in-phase traveling wave-based whole *body undulation*, with wave number K close to unity and, second, antiphase traveling wave-based *surface undulations* with larger values of K . Figure 1 shows the two types of traveling wave-based motion with a variation in the amplitude of the traveling wave along the streamwise (x) direction. In the context of the biolocomotion, Essapian [28] studied waves and wrinkles produced on the dolphin’s skin while catching its prey. In previous numerical studies, the varying amplitude $a(x)$ is modeled as linear [18], quadratic [29], and exponential [30] for the body undulation while the surface undulation considers $a(x)$ proportional to the local thickness of the hydrofoil. Thus, $a(x) = 0$ at the leading and trailing edge of the hydrofoil for the surface undulation while, for the body undulation, the amplitude is zero at the leading edge and maximum at the trailing edge. A literature survey on both types of traveling wave-based motions is presented below.

For free-stream flow across a traveling wave-based *body undulation* of a hydrofoil, Thekkethil *et al.* [18], from our research group, proposed a generic kinematic model where the body undulations asymptote to body pitching with increasing wavelength λ^* of the traveling wave. Further, they found that the pitching motion provides larger thrust while undulation offers larger propulsive efficiency. Manjunathan and Bhardwaj [11] compared the effect of pitching and heaving of an elastic plate. For pure pitching, they found that the rigid as compared to the flexible plate is more efficient for larger pitching frequencies, while the flexible plate behaves similar to the rigid plate for lower pitching frequencies. For a flexible heaving plate, Goza *et al.* [16] showed the role of resonance on propulsive performance. They showed that the thrust is maximum near the resonant frequency for both small and large amplitude heaving motions. The maximum propulsive efficiency is near the resonant frequency for small amplitudes and far from the resonant frequency for large amplitudes.

For a free-stream flow across a traveling wave-based body undulation of a plate, Taneda and Tomonary [31] experimentally found that the flow separation occurs when the wave speed c of the wave on the plate is smaller than the free-stream flow velocity u_∞ . For $c > u_\infty$, they found that the streamlines emanate from one surface of the wave and end on the other. Ivashchenko *et al.* [32] computationally found a steady vortex formation in the trough of the in-phase traveling wave-based surface undulation on a hydrofoil. Recently, Akbarzadeh and Borazjani [33] computationally showed that flow separation does not solely depend on the wave speed c of a traveling wave-based body undulation on an inclined plate. The wave speed can be changed by either changing the frequency or wavelength of the wave. They found that an increase in the wave speed by increasing frequency behaves differently than that of decreasing wavelength for the purpose of reducing the

flow separation. Using direct numerical simulation (DNS) for streamwise traveling wave-based undulation of a wall, Shen *et al.* [34] observed an enhanced flow separation for an upstream traveling wave (i.e., $c/u_\infty < 0$) and also for downstream wave motion (i.e., $c/u_\infty > 0$) at $c/u_\infty < 1$ whereas, for $c/u_\infty > 1$, the reattachment of the flow occurs for the downstream wave motion.

Previous studies on the traveling wave-based *surface-undulations* are motivated by the waves or wrinkles recorded on the skin of a fast-moving dolphin [28], which could be a thrust generation strategy of the dolphin. Motivated by these wrinkles, Xu *et al.* [35] and Wu *et al.* [36] found that the antiphase traveling wave-based surface undulations on the leeward side of the cylinder can be used to suppress the von Kármán vortex street behind the cylinder. Wu *et al.* [36] focused on the reduction of drag on a bluff body using traveling wave motion on the surface of the body. Similarly, Jones *et al.* [37] employed a standing wave on the suction side of the hydrofoil at $Re = 50\,000$ and reported that the stall is delayed due to the triggering of boundary layer instability and the lift-to-drag ratio increases by 40% with a different actuation frequency. In another study, Thompson and Goza [38] studied the effects of traveling wave-based surface undulation on the lift at low and stalled angles of attack. They reported that the lift increases because of the prescribed surface undulation due to the changes in the streamline curvature which in turn changes the pressure distribution on suction side of the foil.

Sooraj *et al.* [39] in their work suggested that a corrugated airfoil is more efficient than a normal airfoil due to the formation of vortices in the grooves of the corrugated airfoil, which is similar to the upper surface undulation of a virtual airfoil. These trapped vortices work as a roller bearing, as explained by Chuijie *et al.* [40]. Chuijie *et al.* [40] defined the concept of fluid roller bearing, where trapped clockwise (CW) vortices in the trough of the streamwise traveling wave on a body surface serve as a roller bearing which reduces drag on the body. They focused on the delay of stall using traveling wave motion on certain parts of the upper surface of the hydrofoil. Akbarzadeh and Borazjani [41] also confirmed the delay in stall of an inclined airfoil undergoing a traveling wave-based upper surface-undulation at $Re = 5 \times 10^4$ whereas, for traveling wave-based both top and bottom surface undulation of a hydrofoil, Tian *et al.* [42] numerically analyzed self-propulsion of a NACA0012 hydrofoil. They found that the mean forward velocity of the hydrofoil increases with the amplitude, wave speed, and wave number of the traveling wave. In follow-up work, Tian *et al.* [43] compared the final mean cruising velocities of self-propelled single wave-number-based body undulation with the larger wave number-based surface-undulations, which are 0.58 and 0.52 times the wave speed, respectively.

The above literature review shows that there are numerous works on the body-undulation waves for a hydrofoil, with wave number k close to unity [Fig. 1(a)] while almost no such work is found for the surface undulations [Fig. 1(b)], except Tian *et al.* [42,43], with a limited parametric study. Further, for similar surface undulations on the leeward side of the cylinder, a couple of works are available that mainly focus on reducing the drag and VIV of the cylinder. Thus, the objective of the present paper is to explore the impact of traveling waves on the surface of a hydrofoil and to perform a detailed parametric study on the effect of nondimensional phase speed c^* , local amplitude-thickness ratio A_L , and Reynolds number Re on the flow characteristics and propulsive performance. Our study is designed to investigate the following research questions: (i) What is the mechanism for the thrust generation and the transition from drag to thrust? (ii) How does the thrust vary spatially along the timewise varying wavy surface? (iii) How does the mechanism and magnitude of thrust generation for the surface undulations compare with that for body undulation in the literature? (iv) What are the various flow regimes, based on streamwise velocity and vorticity patterns, under the effect of surface undulations in a free-stream flow?

II. PHYSICAL AND COMPUTATIONAL DESCRIPTION OF PRESENT PROBLEM

Figure 2 shows the present problem on a free-stream flow across a NACA0012 hydrofoil that undergoes streamwise traveling wave-based surface undulations. Note from the figure that the undulation at the top and bottom surfaces are antiphase. Also note that the amplitude $a(x)$ of the

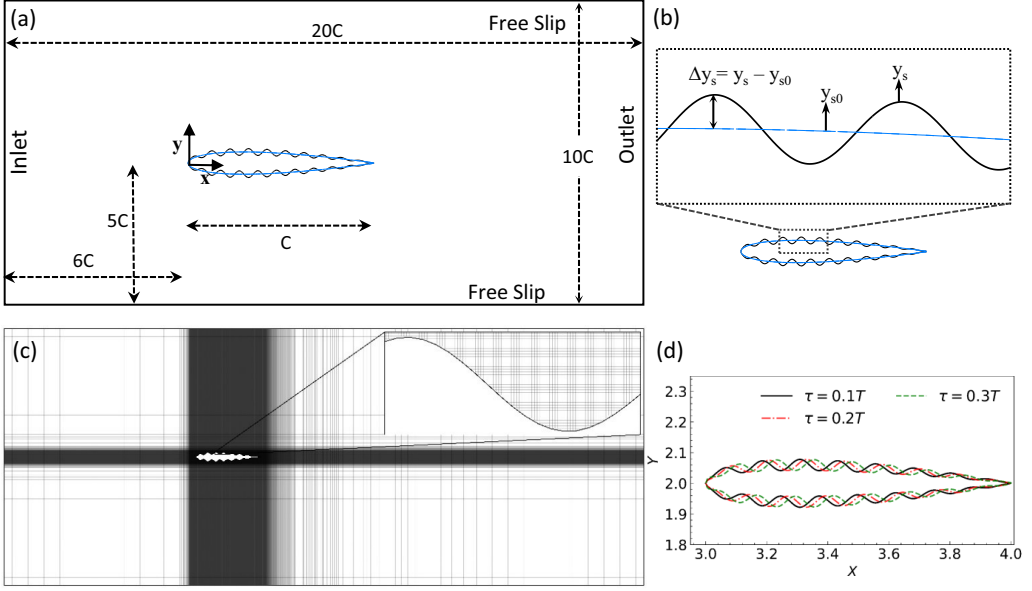


FIG. 2. (a) Computational setup for free-stream flow across a traveling wave-based surface undulation of NACA0012 hydrofoil. (b) Zoomed-in view, where y_{s0} and y_s are y coordinates of the hydrofoil without and with surface undulations, respectively. (c) Computational grid along with a zoomed-in view of the grid near the hydrofoil. (d) Timewise variation of the surface undulations of the hydrofoil, where T is the time period of the traveling wave.

wave varies along the streamwise (x) direction, with an *increasing-decreasing* trend, and is zero at the leading as well as trailing edge. The variation in amplitude over the hydrofoil, with zero amplitude at the leading and trailing edge, is motivated by the propulsion of stingray fish, who undulate their bodies with zero amplitude at both ends [44].

Kinematic model for the traveling wave-based surface undulations of the hydrofoil is given below:

$$y_s(x, t) = y_{s0}(x) + a(x)\sin[2\pi(kx - ft)], \quad (1)$$

where y_{s0} is the y coordinate of the surface or profile of the undeformed hydrofoil and $a(x)$ is the streamwise varying amplitude of the wave. Compared to previous studies [37,38,41,45,46] that focused on the surface undulation on suction or the upper side of the hydrofoil, we consider actuation on both the pressure and suction surfaces of hydrofoil since the focus of the present paper is on thrust generation.

Also, considering λ as the wavelength and T as the time period of the traveling wave, $k = 1/\lambda$ is the wave number and $1/T$ is the frequency of the wave. The amplitude $a(x)$ is modeled such that it is directly proportional to $2y_{s0}$, i.e., the local thickness of the hydrofoil. Thus, the amplitude $a(x)$ is given as

$$a(x) = 2A_L y_{s0}, \quad (2)$$

where A_L is the local amplitude-thickness ratio, defined as the ratio of the local amplitude and the local thickness. The resulting amplitude $a(x)$ is zero at the leading edge and trailing edge while $a(x)$ is maximum at the maximum thickness ($0.12C$); corresponding to 30% of the chord length C ($0.3C$) for the present NACA0012 hydrofoil as seen in Fig. 2.

Considering chord length C as the length scale and u_∞ as the velocity scale, the nondimensional form of the Eq. (1) is given as

$$\Delta Y_s = Y_s(X, \tau) - Y_{s0}(X) = 2A_L Y_{s0} \sin[2\pi K(X - c^* \tau)], \quad (3)$$

where $Y_s = y_s/C$; $Y_{s0} = y_{s0}/C$; $X = x/C$ and $\tau = Ct/U_\infty$ is nondimensional time. Note that the phase difference between the top and bottom surface undulations is kept constant at 180° for all simulations. Further, c^* is the nondimensional phase speed, K is the nondimensional wave number of the traveling wave, and A_L is the local amplitude-thickness ratio of the traveling wave-based top and bottom surface undulations; defined as follows:

$$c^* = \frac{f\lambda}{u_\infty} = \frac{c}{u_\infty}; K = \frac{C}{\lambda} \text{ and } A_L = \frac{a(x)}{2y_{s0}}. \quad (4)$$

The computational domain, along with the boundary conditions (BCs), is shown in Fig 2. The inlet is prescribed with a free stream velocity u_∞ . Free slip BC is used at the top and bottom boundaries, no-slip BC is used on the hydrofoil, and a convective BC (with convective velocity U_c is equal to one) is used at the outlet. The nondimensional BCs are given as $U = 1$, $V = 0$, and $\partial P/\partial X = 0$ at the inlet; $\partial U/\partial Y = 0$, $V = 0$, and $\partial P/\partial Y = 0$ at the top and bottom boundaries; $\partial U/\partial \tau + U_c \partial U/\partial X = 0$ and $P = 0$ at the outlet, and $U = 0$, $V = V_s$, and $\partial P/\partial n = 0$ (where n is the normal to the body surface) on the hydrofoil surface. Here, V_s is the nondimensional velocity in the y direction, obtained by differentiating Eq. (3) with respect to time:

$$V_s = -Kc^*A_L Y_{s0}(X) \cos[2\pi K(X - c^* \tau)]. \quad (5)$$

Figure 2(c) shows a *nonuniform* Cartesian grid used in the present paper, where the smallest grid size δ is used near the hydrofoil, the largest grid size Δ is used away from the hydrofoil, and a hyperbolic stretching is done in between the δ and Δ for the intermediate region. After a grid-size independence study, presented below, a nonuniform Cartesian grid with $\delta = 0.001$ and $\Delta = 0.25$ is selected for all the present simulations, shown in Fig. 2(c). Inset in the figure shows a zoomed-in view of the finest uniform grid $\delta = 0.001$ near the hydrofoil surface. Figure 2(d) shows a timewise variation of the instantaneous shape of the wavy hydrofoil based on the traveling wave-based surface undulations.

III. MATHEMATICAL, NUMERICAL, AND PARAMETRIC DETAILS

A. Governing equations and numerical methodology

The fluid flow is governed by unsteady form of continuity and Navier-Stokes equations, given as

$$\nabla \cdot \mathbf{U} = 0, \quad (6)$$

$$\frac{\partial \mathbf{U}}{\partial \tau} + \nabla \cdot (\mathbf{U}\mathbf{U}) = -\nabla P + \frac{1}{\text{Re}} \nabla^2 \mathbf{U}, \quad (7)$$

where $\mathbf{U}(= \mathbf{u}/u_\infty)$ is the nondimensional velocity vector, $P(= p/\rho u_\infty^2)$ is the non-dimensional pressure, and $\text{Re}(= \rho u_\infty L/\mu)$ is the Reynolds number. Here, ρ is the density and μ is the viscosity of the fluid. The nondimensional time τ is defined as tu_∞/C .

The present prescribed motion-based moving boundary problem is solved using a one-way coupled fluid-structure interaction solver based on a level set-based immersed interface method (LS-IIM) [47]. In the LS-IIM, the interface between the solid and fluid is captured using a level-set function—a normal signed distance function from the interface. The level-set function is updated after each time step using minimum distance and winding algorithms [47] governed by the predefined surface undulations; presented above. The LS-IIM is a finite volume-based method that utilizes a fully implicit pressure projection method on a co-located grid. QUICK scheme is used for the advection term of Navier-Stokes equations, and central difference scheme is used for the diffusion term. Further details on the LS-IIM are available in Thekkethil and Sharma [47,48].

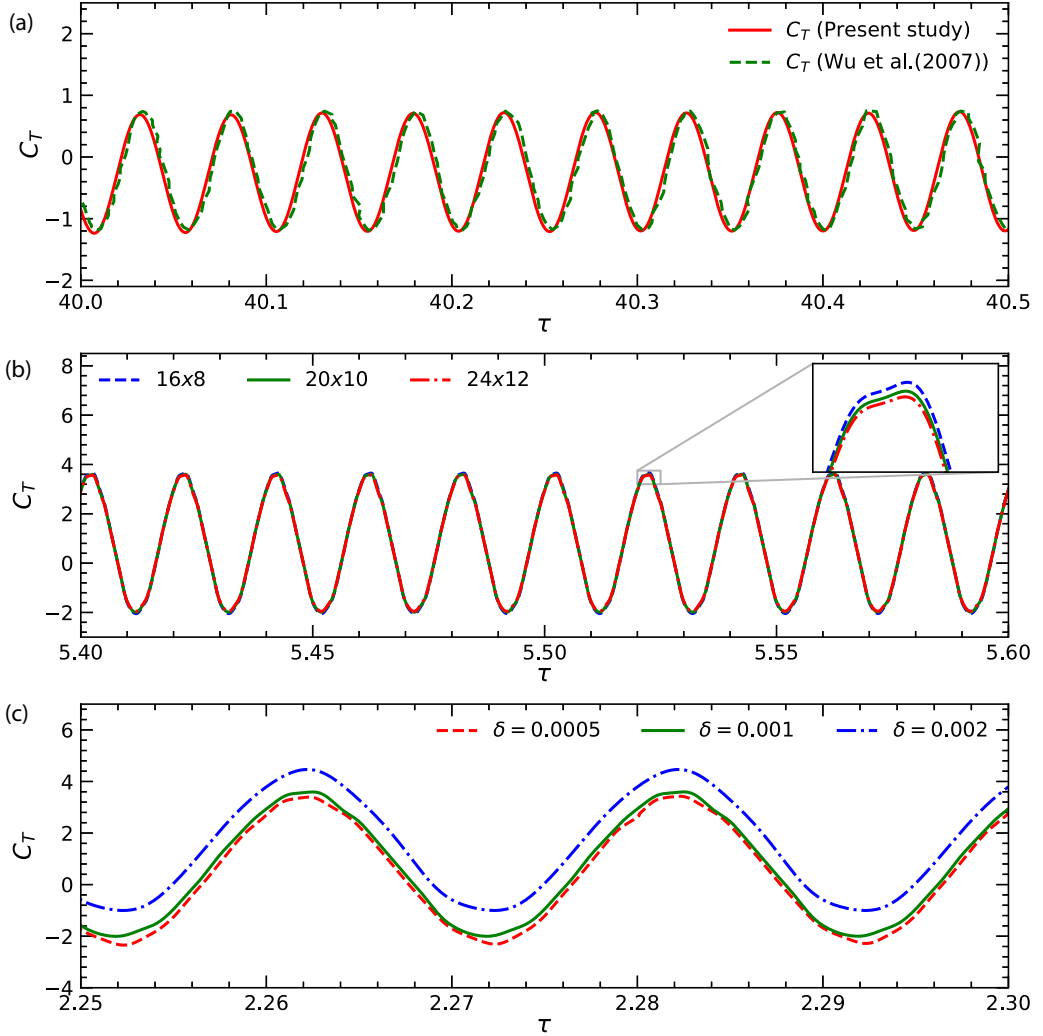


FIG. 3. (a) Validation of the in-house code, (b) domain-size independence, (c) grid independence studies, for temporal variation of thrust coefficient C_T .

B. Code validation and domain size as well as grid independence studies

For the present LS-IIM-based FSI solver, Thekkethil and Sharma [47] presented a detailed code-validation study for various problems. For a problem close to the present paper, a validation study is presented here for traveling wave-based surface undulations on the leeward side of the cylinder in a free-stream flow. Figure 3(a) shows excellent agreement between the present and published [36] results for the temporal variation of the coefficient of thrust at $Re = 5000$, nondimensional phase speed $c^* = 4$, nondimensional wave number $K = 4$, and nondimensional maximum amplitude A_{\max} as 0.02.

For the domain-size independence study on the present problem, Fig. 3(b) shows an almost same temporal variation of thrust coefficient C_T on a nondimensional domain size of 20×10 and 24×12 and a slightly larger value of the peak value of C_T on a smaller domain size of 16×8 . Thus, the domain size of 20×10 is used in the present simulations. Further, considering smallest values of finest grid $\delta = 0.0005$ (used near hydrofoil with the above discussed coarser nonuniform grid far

TABLE I. Parametric details for the present numerical study.

Governing parameters	Parametric values	
	Variable	Constant
Local amplitude-thickness ratio: A_L	0.05, 0.1, 0.15, 0.2, 0.25	Re = 5000
Reynolds number: Re	100, 500, and 1000–5000 (in steps of 10^3)	$A_L = 0.15$

Nondimensional phase speed c^* is also varied from 1–10 (in step of 1) for the above parametric study on various A_L and Re. Note that the wave number $K = 10$ for all simulations.

away), Fig. 3(c) shows that the difference in the temporal variation of C_T reduces substantially with grid refinement, i.e., the difference between the results on $\delta = 0.0005$ and $\delta = 0.001$ is much smaller than that between the results on $\delta = 0.0015$ and $\delta = 0.002$. Thus, considering $\delta = 0.001$, a grid size of 1589×506 is used in the present simulations. The time step used in the present paper is $\delta\tau = 1/(200Kc^*)$, i.e., the 200th part of the nondimensional time period of the wave that varies from 10^{-4} to 10^{-5} ; obtained after a time-independence study.

C. Selection of parameters and parametric details

The present paper focuses on the effect of the traveling wave-based surface-undulations on the mechanism of thrust generation for a NACA0012 hydrofoil in free-stream flow. Further, a detailed parametric study is done for the effect of various traveling wave-based parameters (c^* and A_L) with wave number $K = 10$ on the thrust generation and propulsive efficiency at various Re. The simulated values of the governing parameters are presented in Table I. The justification of the values of the governing parameters is as follows. In the work of Essapian [28], roughly ten waves were recorded on the surface of a dolphin. Similarly, in previous numerical works on surface undulations, the wave number K was 2.27 in Ref. [46], 5 in Ref. [41] and 8 in Ref. [42]. Thus, we consider a wave number (K) of 10, that is representative of data reported in prior studies.

The ratio of undulation wave amplitude and fin width for various stingray fish varies from 0.08–0.35, as reported by Rosenberger [44]. These fishes undulate their bodies with zero amplitude at both ends. On the other hand, for body undulation, the ratio of tail-beat amplitude to chord length lies in the range of 0.08–0.35 for different fish such as mackerel [49], bluefin tuna [50], and sturgeon [51]. In the present paper, we consider the ratio of wave amplitude and foil thickness in the range of 0.05–0.25 as shown in Table I, which is representative of the above-mentioned data of fish. The table shows that the maximum Re considered here is 5000, which falls in the low Re range for laminar flow over NACA0012 hydrofoil, reported in an experimental study by Alam *et al.* [52].

The propulsive performance of surface-undulating hydrofoil is investigated with the help of certain parameters: mean thrust coefficient $\langle C_T \rangle$ and propulsive efficiency η_p . This section presents the formulation of $\langle C_T \rangle$ and η_p , which are similar to that used in present works from our research group [18,53]. However, a power-loss coefficient [2] is also considered in the present paper to quantify the rate of viscous dissipation; presented below.

Coefficient of thrust C_T is given as

$$C_T = \frac{F_T}{\frac{1}{2}\rho u_\infty^2 C}, \quad (8)$$

where F_T is the instantaneous thrust force on the hydrofoil. Further, a time-averaged or mean thrust coefficient is given as

$$\langle C_T \rangle = \frac{1}{T} \int_\tau^{\tau+T} C_T(\tau) d\tau, \quad (9)$$

where $\langle \rangle$ denotes quantities that are averaged over time. The time averaging is done for 20 cycles of traveling wave motion. Input power for surface undulation is given [18] as

$$P_{\text{in}} = \oint_S f_L v_s ds, \quad (10)$$

where f_L is the local lateral force per unit surface area of the hydrofoil, v_s is the lateral velocity of the traveling wave, and ds is a dimensional infinitesimal surface area on the hydrofoil surface. Propulsive efficiency of surface traveling wave motion is given as

$$\eta_p = \frac{P_{\text{out}}}{P_{\text{in}}} = \frac{\langle F_T \rangle u_\infty}{\langle P_{\text{in}} \rangle} = \frac{\langle C_T \rangle}{\langle \int c_L V_s dS \rangle} = \frac{\langle C_T \rangle}{\langle C_P \rangle}, \quad (11)$$

where c_L is the local lift coefficient on the hydrofoil per unit surface area, V_s is the nondimensional lateral velocity of the traveling wave, and $\langle C_P \rangle$ is the mean coefficient of input power; required for the surface undulations. Here, dS represents a nondimensional infinitesimal surface area on a hydrofoil surface.

Arakeri and Shukla [2] presented a net power loss P_L as the difference of the input-power P_{in} and the output-power P_{out} due to thrust production. Thus, P_L is given as

$$P_L = P_{\text{in}} - P_{\text{out}} = P_{\text{in}} - \langle F_T \rangle u_\infty. \quad (12)$$

A nondimensional form of the above equation is given as

$$C_{PL} = \langle C_P \rangle - \langle C_T \rangle = (1 - \eta_p) \langle C_P \rangle, \quad (13)$$

where C_{PL} is the power-loss coefficient which is also equal to the sum of the rate of kinetic energy left behind in the wake (\dot{W}) and the rate of viscous dissipation (Φ_v), as explained by Arakeri and Shukla [2] and given as

$$C_{PL} = \dot{W} + \Phi_v. \quad (14)$$

To compute \dot{W} , we consider a control volume (CV) Ω . The right boundary of the CV is at a distance of $0.5L$ from trailing edge of the hydrofoil. Using the formulation given by Arakeri and Shukla [2], \dot{W} is given as

$$\dot{W} = \frac{1}{\rho u_\infty^3 C} \int_{-b}^b \rho u ((u_\infty - u)^2 + v^2) dy, \quad (15)$$

where u and v are dimensional velocities in the x and y directions at the outlet boundary (Ω_R) of the CV, respectively. Further, b represents the extent of the control volume Ω in the y direction from the center line of the hydrofoil. Substituting from Eqs. (14) and (15), Eq. (13) results in a rate of viscous dissipation as

$$\Phi_v = (1 - \eta_p) \langle C_P \rangle - \int_{-B}^B U ((1 - U)^2 + V^2) dY. \quad (16)$$

IV. MECHANISM OF THRUST GENERATION BY SURFACE-UNDULATIONS

Figure 4 shows the effect of various phase speeds c^* on instantaneous contours and profiles of U velocity and vorticity. The profiles correspond to the transverse variation of the U velocity and vorticity at a streamwise location (from hydrofoil's leading edge) $X_{LE} = C, 1.25C$ and $1.5C$ at and behind the trailing edge of the hydrofoil. The insets in the figure show a zoomed-in view of the contours; close to the upper surface of the hydrofoil for both U -velocity and -vorticity contours. Here, a mechanism of thrust generation is presented with the help of flow patterns near the upper surface of the hydrofoil; a similar argument applies to the lower surface of the hydrofoil.

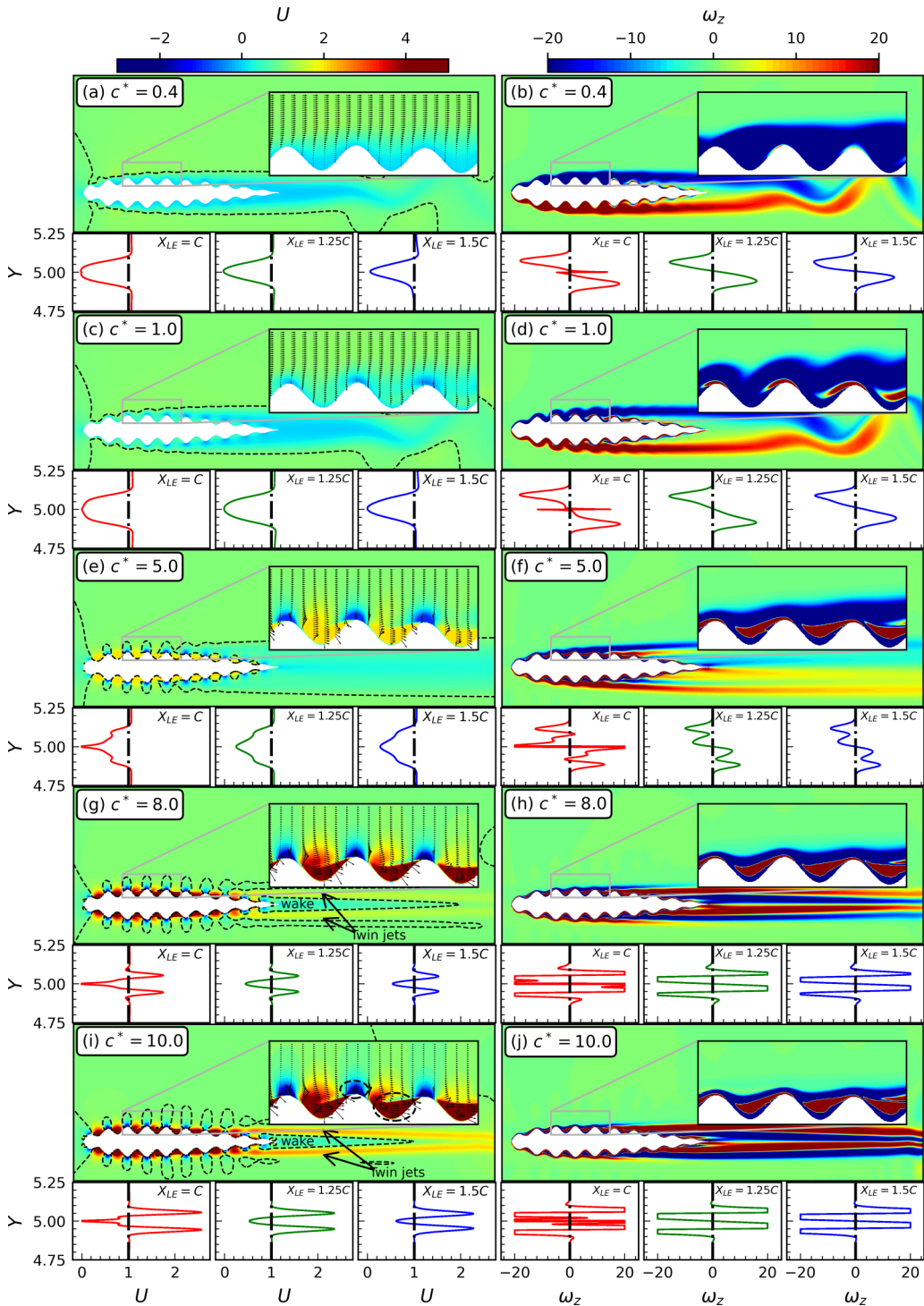


FIG. 4. Instantaneous U -velocity contours (left column) and vorticity contours (right column), above the U -velocity and -vorticity profiles behind the hydrofoil, for various phase speeds c^* at amplitude-thickness ratio $A_L = 0.15$, wave number $K = 10$, and $Re = 5000$. For (a, c, e, g, i), the velocity vectors are shown in the insets and a dotted line corresponds to $U = 1$. For (b, d, f, h, j), the insets show vorticity field near the hydrofoil's surface.

For a lower traveling wave phase speed $c^* = 0.4$, the inset view in Fig. 4(a) shows an almost zero U velocity while Fig. 4(b) shows a negative or CW vorticity in both the trough and crest regions of the wavy surface of the hydrofoil. However, for a larger $c^* = 0.7$, the streamwise U velocity increases in the trough of the wavy hydrofoil and becomes mostly positive [Fig. 4(c)] while the vorticity in the crest of the wavy hydrofoil becomes positive or counterclockwise (CCW) [Fig. 4(d)]. Thus, with an increase in the phase speed c^* , for 0.4 and 0.7, the deceleration of the free-stream flow in the trough region reduces, and the flow near the hydrofoil is not able to keep up with the increased phase speed of the traveling wave that leads to a reversed flow, flow separation, and CCW vorticity at the crest of the wavy hydrofoil. For the phase speed less than free-stream velocity ($c^* \leq 1$), the flow pattern in the trough of the wavy surface shows that the streamwise velocity is significantly less than the free-stream velocity u_∞ , and the CW vorticity is found in the trough regions. In contrast, for $c > u_\infty$ or $c^* > 1$, the streamwise velocity $u > u_\infty$ ($U > 1$) in the trough of the wavy surface as shown in Figs. 4(g) and 4(i), and the CCW vorticity starts to appear in the trough region as shown in Figs. 4(h) and 4(j). Further, for $c^* > 1$, the figure shows an accelerated flow ($U > 1$) at the trough and a decelerated flow ($U < 1$) at the crest of the wave [indicated by an encircled dashed line in the inset of Fig. 4(i)]; here, the acceleration and deceleration of the flow are with respect to the free-stream velocity.

At the larger c^* , the accelerated flow ($U > 1$) in the trough gets advected downstream by the streamwise traveling wave, which produces *twin jets* behind the hydrofoil—one each by the upper and lower surface undulations. This is seen behind the hydrofoil in the U -velocity contours and velocity profile for $c^* = 8$ and 10 in Figs. 4(g) and 4(i), respectively. Similarly, for vorticity contour, Figs. 4(h) and 4(j) show four vortex sheets—two or twin vortex sheets generated by each of the surface undulations.

A line contour for streamwise velocity $U = 1.0$ in Figs. 4(a), 4(c) 4(e), 4(g), and 4(i) demarcates the wake ($U < 1$) and jet ($U > 1$) for the flow field behind the hydrofoil. The figure shows that the wake region behind the hydrofoil decreases with increasing phase speed c^* . A twin jet is visible behind the hydrofoil along with the localized accelerated flow ($U > 1$) in the trough of the wave, for $c^* = 10.0$, shown in Fig. 4(i). These twin jets start to form at $c^* = 7$. A change in the sign of the vorticity across the above discussed forward/reverse twin vortex sheet is also shown by the vorticity profile behind the hydrofoil in Fig. 4, at various phase speeds c^* .

Due to the traveling wave-based surface undulations, the downward region or rear side for each of the hatlike wavy surfaces pushes the surrounding fluids while its upward region or front side sucks the nearby fluid. Thus, for each of the hatlike wavy surfaces, a larger pressure on the rear side (as compared to the front side) results in a net thrust force. Thus, the surface-undulation-based thrust generation is distributed over each wave of the wavy surface, with suction and pressure cycles on the front and rear side of each hatlike wavy surface; shown schematically in Fig. 5. Thus, the traveling wave-based surface-undulation leads to the pressure-suction mechanism for the thrust generation. This mechanism was also reported by Müller *et al.* [54] and Thekkethil *et al.* [18] for a single traveling wave-based body undulation of a fish and hydrofoil, respectively. Thus, each of the upper and lower surface undulations at larger c^* leads to one jet flow and twin-vortex sheets. These twin-vortex sheets are called here *reverse* since the opposite-signed CCW above CW vortex sheets induces the jet flow in the upper and lower halves, shown schematically in Fig. 5. The figure also shows the inner twin-vortex sheets, sandwiched between the outer twin-vortex sheets, as the *forward* twin-vortex sheets (FV_{sheet}), which induces the wake flow in between the CW above the CCW vortex sheets. The proposed classification of the twin-vortex sheets as forward and reverse is motivated by a similar classification of a von Kármán vortex street—well reported for the body-undulation of a hydrofoil [18]. The forward von Kármán vortex street (FV_{street}) is also found in the present problem at low phase speed c^* , as shown in Figs. 4(b) and 4(d) for $c^* = 0.4$ and 1.0. Further, instead of the two reverse twin-vortex sheets (RV_{sheet}), two reverse von Kármán vortex streets RV_{street} [above and below a forward von Kármán street (FV_{street})]; is presented below in Fig. 10(k) for $A_L = 0.2$, $c^* = 8$, $K = 10$ and $Re = 5000$. Thus, the large c^* -based upper and lower surface undulations lead to one forward and two reverse twin-vortex sheets or vortex streets.

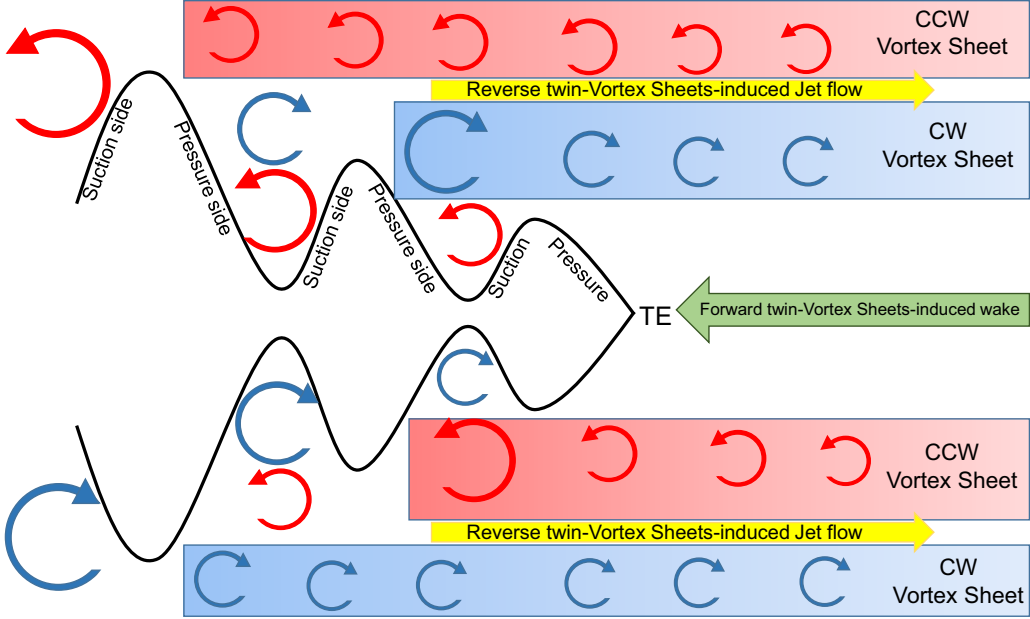


FIG. 5. Schematic for the pressure-suction mechanism and the formation of two pairs (2Ps) of reverse vortex sheets and one pair of forward vortex sheets, which induces jet flow and wake flow sandwiched between each pair of the respective vortex sheets.

V. EFFECT OF PHASE SPEED C^*

A. Flow characteristics

Figure 6 shows streamlines for a timewise steady and varying shape of the hydrofoil, at $c^* = 0$ and $c^* > 0$, respectively. For the corrugated or wavy hydrofoil (at $c^* = 0$), Fig. 6(a) shows that isolated vortices get trapped in the trough of the wave.

For $c^* = 0.4-1.0$, Fig. 6(a) shows a vortex shedding behind the hydrofoil. The effect of the surface undulations becomes *localized* near the hydrofoil and the overall streamwise flow slightly further from the body becomes streamlined for phase speed $c^* \geq 2$ of the traveling wave. To discern the recirculation pattern for $c^* > 0$, Fig. 6(b) shows streamlines in a moving frame of reference with respect to the wave speed c^* . This moving reference frame makes the flow stationary on the wavy surface, and the resulting streamlines in Fig. 6(b) show prominently forward flow for $c^* < 1$, reversed flow for $c^* > 1$, and the counter-rotating flow regime-based twin vortex on the hydrofoil at $c^* = 1$. The figure shows isolated vortices in each trough for $c^* < 1$, and the isolated vortices move away from the wavy surface of the hydrofoil with increasing $c^* (< 1)$ as shown in Fig. 6(b) for $c^* = 0.7$. This leads to the dominance of the free-stream velocity-based forward flow, which leads to downstream advection of the isolated vortices as compared to an upstream advection by the reversed flow near the wall [Fig. 6(b) for $c^* = 0.7$]. For $c^* > 1$, the streamlining and reversed flow in Fig. 6(b) are due to the negative sign of relative flow velocity ($u_\infty - c$). These findings are consistent with Shen *et al.*'s [34] work on flexible walls with traveling waves.

Figure 7 shows the vorticity contours along with streamlines for different phase speeds c^* . For flow over a stationary hydrofoil, Fig. 7(a) shows a streamlined motion and a steady forward twin-vortex sheet FV_{sheet} behind the hydrofoil. For a stationary wavy hydrofoil at $c^* = 0$; Fig. 7(b) shows a forward von Kármán vortex street FV_{street} behind the hydrofoil. With increasing $c^* [0, 1]$, Figs. 7(c) and 7(d) show that the distance between the shed vortices increases due to the traveling wave-based

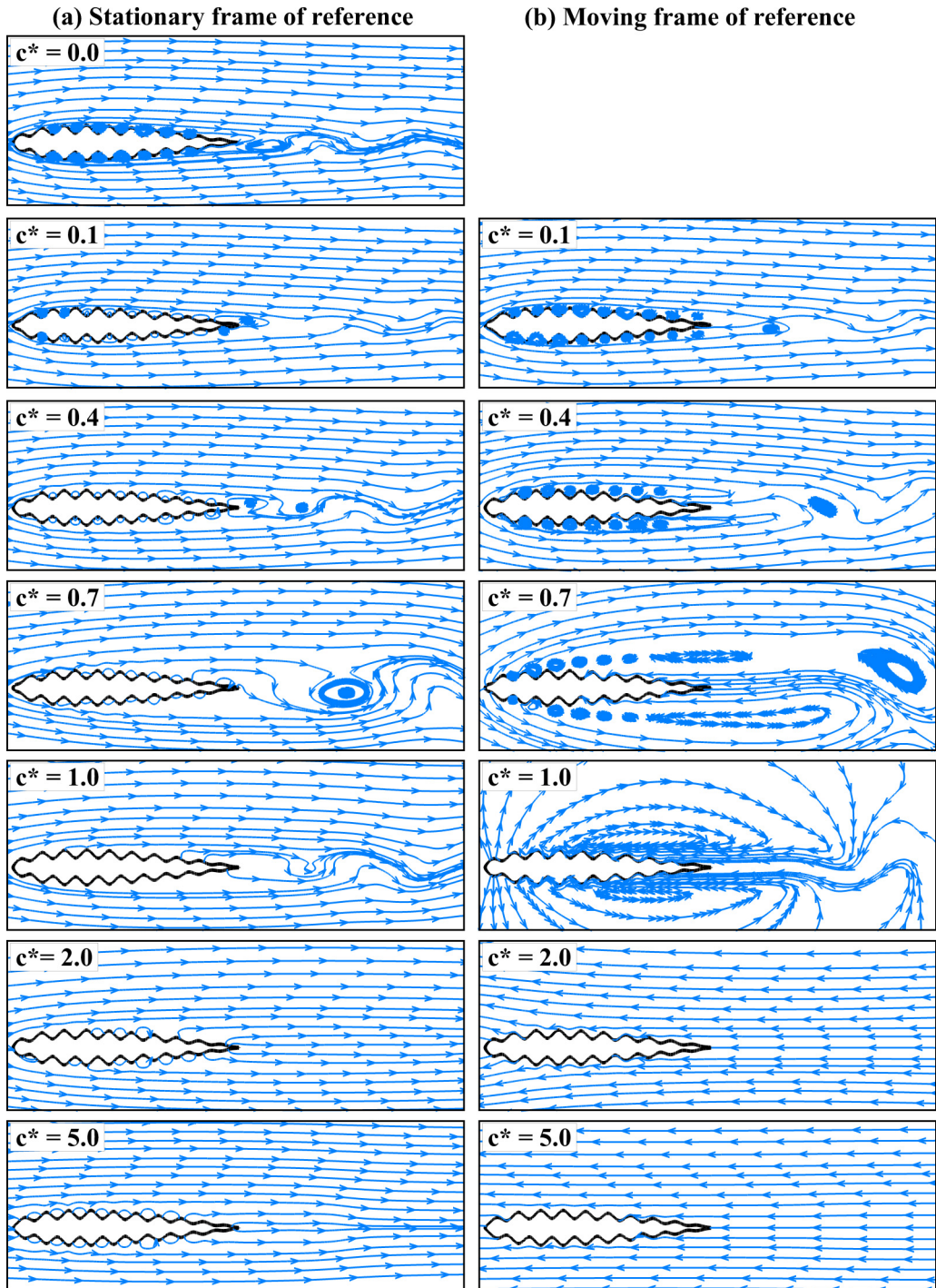


FIG. 6. Instantaneous streamlines in a (a) stationary (b) moving frame with respect to the traveling wave speed for various phase speed c^* at amplitude $A_L = 0.15$, wave number $K = 10$, and $Re = 5000$.

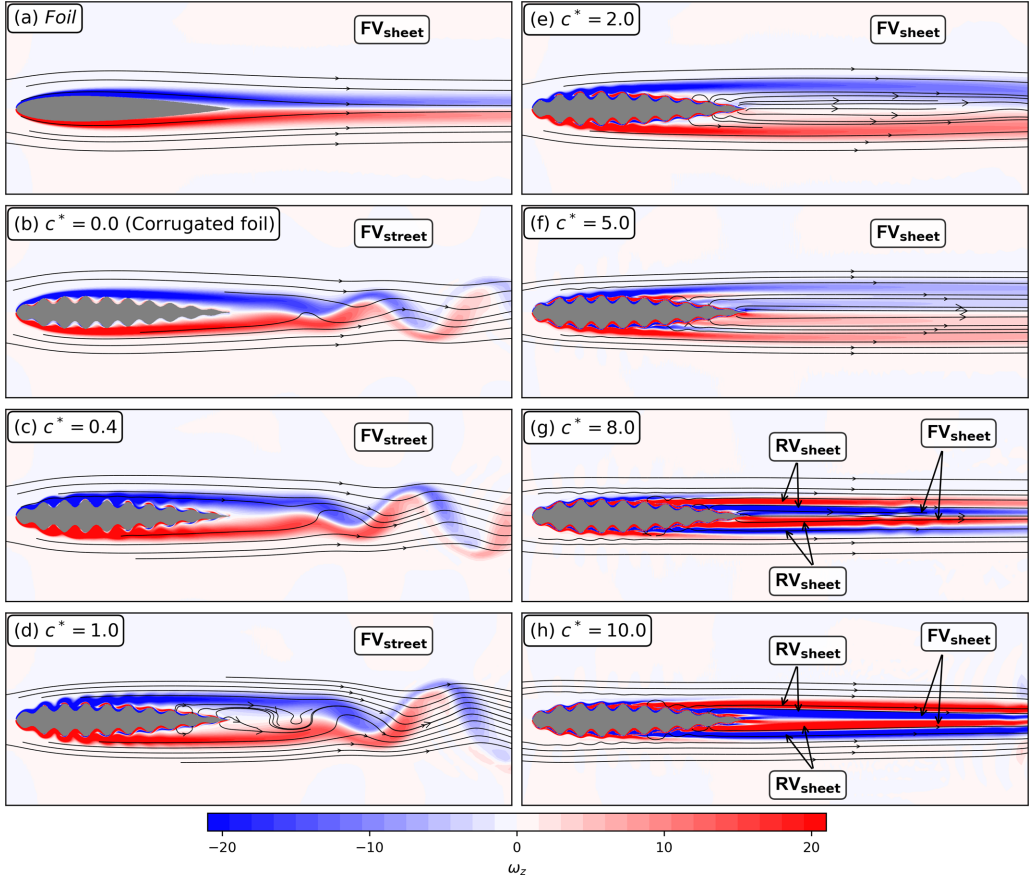


FIG. 7. Vorticity contours and streamlines for free-stream flow across (a) a stationary hydrofoil NACA0012 and (b)–(h) wavy NACA0012 hydrofoil for various c^* at $A_L = 0.15$, $K = 10$, and $Re = 5000$. (b)–(d) show periodic forward von Kármán vortex street (FV_{street}) and almost steady forward vortex sheets (FV_{sheets}) are seen in the other subfigures. Reverse vortex sheets (RV_{sheets}) are also seen in (g) and (h).

streamwise momentum infusion in the wake. These periodic forward von Kármán vortex street FV_{street} disappear as we further increase to the intermediate value of c^* , resulting in an almost steady forward twin-vortex sheet FV_{sheet} as shown in Figs. 7(e) and 7(f) for $c^* = 2$ and 5, respectively. For $c^* = 8$ and 10, Figs. 7(g) and 7(h) show a pair of two almost steady reverse twin-vortex sheets RV_{sheet} —above and below the forward twin-vortex sheet. The increase in phase speed c^* makes the effect of surface undulations on the streamwise flow structure much more localized, and the wavy hydrofoil becomes more streamlined as compared to the $c^* = 0$ case, which acts like a bluff body, as evident from Fig. 7(b). The streamlining of the hydrofoil with surface undulation is explained as follows. For a corrugated foil, the isolated vortices formed in the trough due to flow separation on the rear side of the hatlike wavy surface get advected to the trailing edge of the foil and form FV_{street} . As we apply sufficient excitation phase speed c^* , the flow accelerates inside the trough due to the pressure-suction mechanism as explained in Sec. IV. The momentum imparted due to the surface undulation inhibits the formation of isolated vortices inside the trough. Thus, the increase in phase speed c^* causes the flow to emanate from the front side and fall on the rear side of the wave, supporting the streamwise flow around the foil.

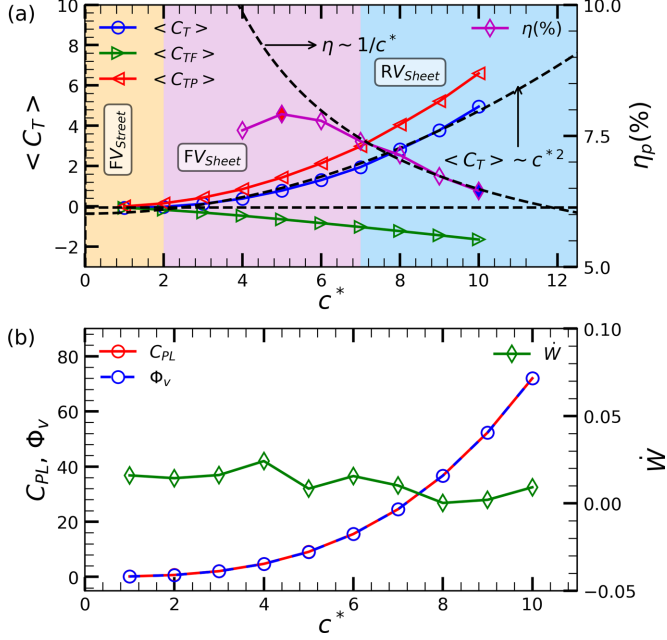


FIG. 8. Variation of (a) mean thrust coefficient, $\langle C_T \rangle$, along with its pressure and viscous component, $\langle C_{TP} \rangle$ and $\langle C_{TF} \rangle$, and propulsive efficiency η_p with increasing phase speed c^* at amplitude $A_L = 0.15$, wave number $K = 10$, and $\text{Re} = 5000$. Power loss coefficient, C_{PL} along with viscous loss (Φ_v), and wake loss (\dot{W}) is shown in (b). The color background in (a) demarcates a periodic forward von Kármán vortex Street (FV_{street} , yellow), steady forward vortex sheet (FV_{sheet} , pink), and steady reverse vortex sheets (RV_{sheet} , blue) in a smaller, intermediate, and large phase speed c^* , respectively. The blue region corresponds to the formation of twin jet in the wake.

B. Thrust coefficient and energy budget

With increasing phase speed c^* , Fig. 8(a) shows an increasing mean thrust coefficient $\langle C_T \rangle$. The figure also shows the pressure and viscous components of the mean thrust coefficient ($\langle C_T \rangle$), with an increasing trend for $\langle C_{TP} \rangle$ and a decreasing trend for $\langle C_{TF} \rangle$. Notice from the figure that the transition from drag to thrust occurs at $c^* = 1.02$, close to $c = u_\infty$, for pressure thrust coefficient ($\langle C_{TP} \rangle$) as compared to that at $c^* = 2.2$ for the total thrust coefficient ($\langle C_T \rangle$). For various c^* , the timewise variation of thrust coefficient is found to reach a periodic variation for $\langle C_T \rangle$ and $\langle C_{TP} \rangle$ while that for $\langle C_{TF} \rangle$ reaches an almost constant steady value (figure not shown).

With increasing phase speeds c^* that lead to a thrust generation, Fig. 8(a) shows a slightly increasing followed by a decreasing trend of variation in propulsive efficiency, with a maximum efficiency $\eta_{p_{max}} = 8\%$ at $c^* = 5$. The colored background in Fig. 8(a) shows a map for flow regimes based on the vorticity patterns behind the hydrofoil; discussed above. The yellow color shows a region for the periodic von Kármán street, and the pink color shows the region with a steady forward twin-vortex sheet region. It is interesting to note that the transition from drag to thrust as well as the maximum efficiency is found in the steady forward twin-vortex sheet regime while the larger thrust coefficient C_T is found in the reverse twin-vortex sheet regime that leads to twin jets.

Figure 8(b) shows an increase in power loss coefficient C_{PL} [Eq. (13)], with increasing c^* . For $c^* > 5.0$, Fig. 8(b) shows that the power-loss coefficient increases sharply in comparison to the ($\langle C_T \rangle$) curve as the efficiency starts to decrease. Figure 8(b) shows that the rate of viscous dissipation Φ_v mainly contributes to the net power loss C_{PL} under the effect of surface undulations, with the kinetic energy left behind in the wake \dot{W} close to zero.

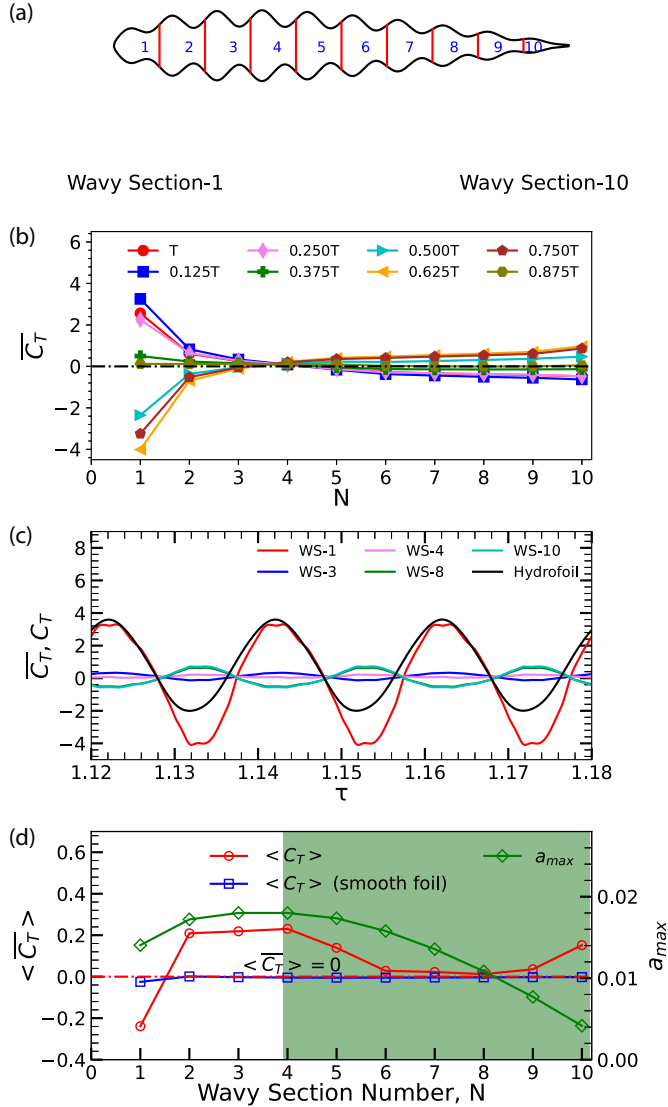


FIG. 9. (a) Ten different equal widths of the timewise varying wavy surface with wave number $K = 10$. (b) Wavy sectionwise variation of the mean thrust coefficient ($\overline{C_T}$) and maximum amplitude a_{max} . (c) Variation of thrust along wavy sections for eight different time instants in one time period. (d) Temporal variation of the thrust coefficient C_T for the various wavy sections at $A_L = 0.15$, $K = 10$, $c^* = 5$ at $Re = 5000$. For (d), the phase difference between the C_T for a section and the net C_T for hydrofoil are 0° (in phase) for $N \leq 3$ and 180° (out of phase) for $N \geq 4$; marked by green color in (b).

C. Wavy sectionwise variation of thrust coefficient

A wavewise spatial variation of a thrust coefficient is presented in Fig. 9 by dividing the hydrofoil into ten different wavy sections for the traveling wave, with wave number $K = 10$, as shown in Fig. 9(a). The instantaneous thrust is spatially averaged over a given wavy section ($\overline{C_T}$), and its

variation along the wavy sections for eight different time instants in an oscillation cycle is shown in Fig. 9(b). Over $T/8$, $\overline{C_T}$ for wavy section 1 increases and becomes maximum, while for the next $T/8$ cycle, $\overline{C_T}$ starts to decrease and becomes almost zero after $3T/8$ of the oscillation cycle. Wavy section 1 contributes to the maximum drag on the body till $7T/8$ and again starts to generate thrust for the remaining $1/8$ cycle, as inferred from Figs. 9(b) and 9(c). Figure 9(c) shows that the $\overline{C_T}$ for wavy sections 3 and 4 are mostly or entirely positive. The oscillation amplitude of $\overline{C_T}$ for the first wavy section ($N = 1$) is larger, and the amplitude is smaller for the other wavy sections. Further, Fig. 9(c) shows that $\overline{C_T}$ is in phase with the net C_T (indicated by a black line) for those sections up to which the thickness of hydrofoil increases (till $X_{LE} = 0.3$), whereas $\overline{C_T}$ is out-of-phase for downstream wavy sections, corresponding to the decreasing hydrofoil thickness. With increasing wavy section number N , Fig. 9(d) shows an increasing-decreasing trend in the variation of the thrust coefficient (C_T). This trend is correlated with a similar trend for the sectionwise maximum local amplitude of the traveling wave, except for the last wavy section $N = 10$, where $\langle C_T \rangle$ increases due to downstream advection of the jet. The time-averaged value for a cycle of thrust ($\langle \overline{C_T} \rangle$) shows that only the first wavy section produces more drag for the surface-undulatory hydrofoil than the smooth hydrofoil (i.e., hydrofoil without surface undulations). Additionally, the white and green backgrounds in Fig. 9(d) show the phase and antiphase trends of $\overline{C_T}$ with the net C_T , respectively, as also shown in Fig. 9(c).

Overall, the time-averaged thrust coefficient signal in Fig. 9(d) shows that the first wavy section creates a drag even though the temporal variation in the half cycle of the first wavy section generates maximum thrust, as shown in Figs. 9(b) and 9(c). The contribution of the first three wavy sections on total thrust is maximum for the first half cycle. The second half cycle generates maximum drag for the first wavy section, which is compensated by the wavy section of $N > 4$ as these are in antiphase to the total thrust, as shown by the green background in Fig. 9(d). The drag is produced for 42% of the cycle. The first three wavy sections contribute to most thrust generation in the first half of the oscillation cycle, while the other remaining wavy sections contribute to the thrust in the other half oscillation cycle.

VI. EFFECT OF LOCAL AMPLITUDE-THICKNESS RATIO AND REYNOLDS NUMBER

This section presents the combined effect of phase speed c^* separately with the nondimensional local amplitude-thickness ratio A_L and Reynolds number Re . The combined effects are presented for the flow patterns and propulsive performance parameters in separate subsections below. Finally, vortex-sheet- and street-based regime maps are presented.

A. Flow patterns

For $c^* = 5-8$ and $A_L = 0.15-0.25$, the streamwise U-velocity profiles in Fig. 10 show jet flows, one each from the top and bottom surface undulations, except for the smaller $A_L = 0.15$ at smaller $c^* = 5$ and 6. For these wake flow cases, forward twin-vortex sheets are formed as shown in Figs. 10(a) and 10(b). Whereas, for the twin jet-flow case, two-pairs (2Ps) of reverse vortex sheets are seen at larger $c^* = 8$ for smaller $A_L = 0.15$ [Fig. 10(j)] and a smaller $c^* = 5$ for larger $A_L = 0.2$ [Fig. 10(b)].

Further, for larger $A_L \geq 0.2$, it is interesting to notice from Fig. 10 a transition in the flow regime from 2P vortex sheets to 2P vortex streets at $c^* = 6$. For the respective vortex pattern, note the transition from the almost steady flow to a periodic flow behind the hydrofoil. The onset of the periodic 2P reverse vortex streets (2P-RV_{street}) leads to meandering twin jets as compared to steady twin jets for the 2P reverse vortex-sheet (2P-RV_{sheet}) regime. At the largest $A_L = 0.25$ simulated here, Figs. 10(f)–10(j) show another transition from 2P-RV_{street} at $c^* = 6$ to a nonperiodic unsteady flow at larger phase speed c^* . An analysis of the nonperiodic flow needs a separate study and is not presented here. With increasing Re , the vorticity contours in Fig. 11 show that the periodic vortices are shed behind the hydrofoil at the smallest $c^* = 1$ while the almost steady vortex sheets

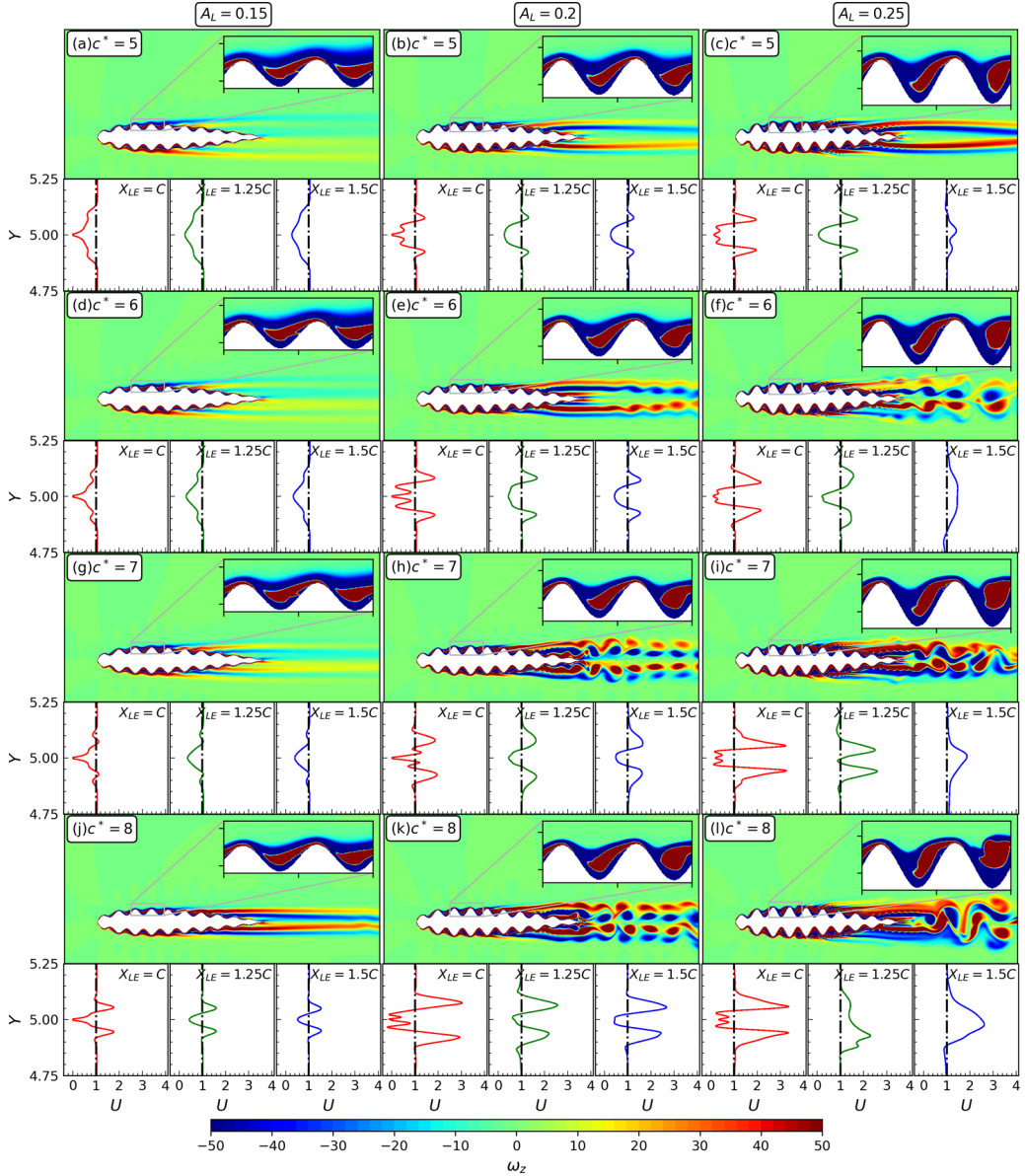


FIG. 10. Instantaneous vorticity contours, above the streamwise velocity profiles behind the hydrofoil, for various amplitude A_L and phase speed c^* at wave number $K = 10$ and $\text{Re} = 5000$.

get elongated at larger c^* . At $c^* = 8$, the velocity profiles show a larger momentum excess and a stronger twin jet, with increasing Re .

B. Propulsive performance

With increasing phase speed c^* , Fig. 12 shows effect of local amplitude-thickness ratio A_L , and Re on the mean thrust coefficient (C_T) and propulsive efficiency η_p . The figure shows an increase in the thrust coefficient (C_T) with increasing c^* , A_L , and Re . Similarly, increase in propulsive efficiency η_p is also seen with increasing A_L , and Re at a constant c^* . Whereas, with increasing c^*

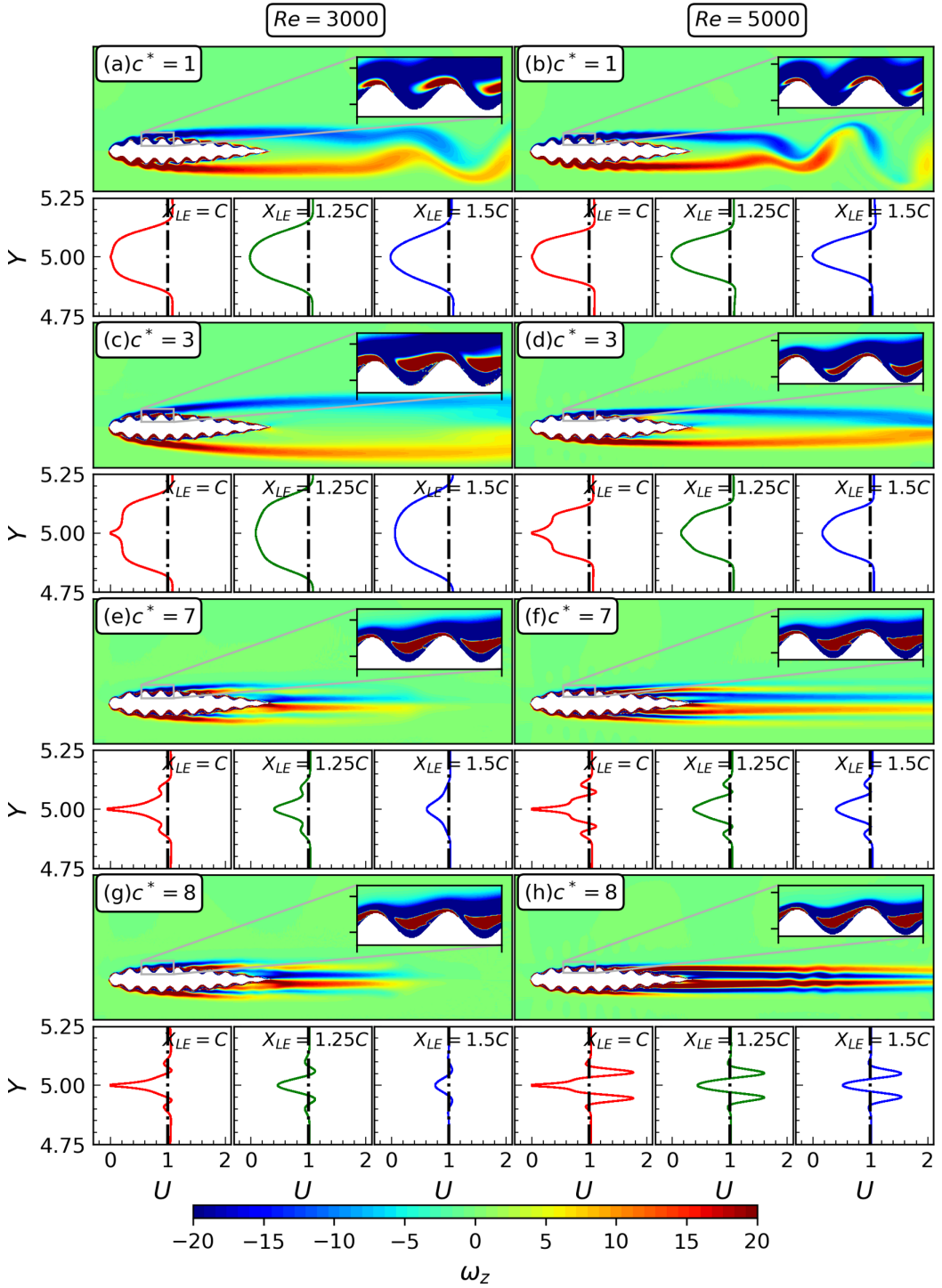


FIG. 11. Instantaneous vorticity contours, above the U -velocity profiles behind the hydrofoil, for various Reynolds number Re and phase speed c^* at amplitude $A_L = 0.15$ and $K = 10$.

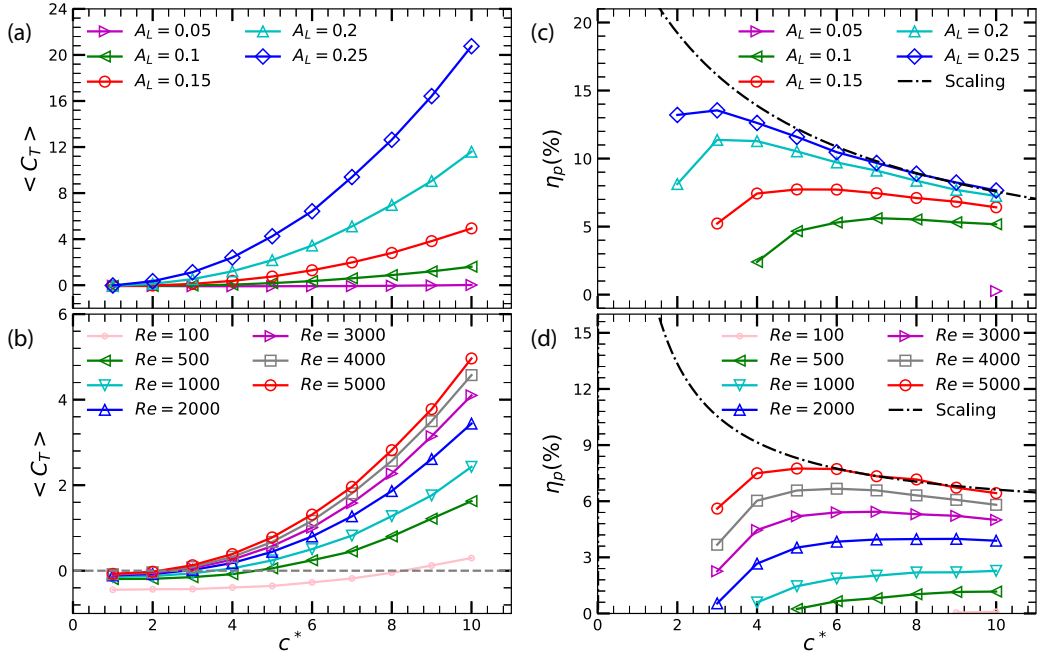


FIG. 12. Variation of (a), (b) mean coefficients of thrust $\langle C_T \rangle$ and (c), (d) propulsive efficiency η_p with increasing phase speed c^* for various amplitudes A_L and Re . The dashed dot line in the efficiency plot corresponds to the proposed scaling for propulsive efficiency ($\eta_p \sim 1/c^*$).

the figure shows an increasing-decreasing trend or an asymptotic increasing trend for η_p at various A_L and Re . For the increasing-decreasing trend, maximum η_p is seen in the figure at a smaller phase speed c^* with increasing A_L and Re . Further, at constant c^* , Figs. 12(c) and 12(d) show that the increment in efficiency η_p reduces with increasing A_L and Re ; vice versa for the increment in the thrust coefficient ($\langle C_T \rangle$) [Figs. 12(a) and 12(b)]. The substantial increase in $\langle C_T \rangle$ (at larger A_L , Re) is attributed to localized region of high velocity in the trough of the wavy surface as well as the twin jets and reverse 2P vortex sheets or reverse 2P von Kármán vortex street forming behind the hydrofoil as shown in Figs. 10(e), 10(f) and 10(h)–10(l).

C. Vortex sheets and street-based regime map

As presented above, the surface undulations in the present problem results in four types of vortex sheets/streets: forward vortex sheet, forward vortex streets, 2Ps of reverse vortex sheet, and 2Ps of reverse vortex street. In addition to these flow regimes, a nonperiodic unsteady flow regime exists at higher values of local amplitude-thickness ratio A_L and phase speed c^* . The various vortex pattern-based flow regimes are presented in a regime map in Fig. 13, for various values of phase speed c^* , local amplitude-thickness ratio A_L , and Re . The figure shows a demarcation of the transition from wake flow to jet flow (black dashed curve in Fig. 13) and from drag to thrust generation (solid black line in Fig. 13). Comparing the above flow pattern and propulsive performance parameter, note that the maximum thrust generation occurs at larger c^* when twin jets and 2P-reverse vortex sheets are formed behind the hydrofoil [Figs. 13(a) and 13(b)], while the efficiency is maximum at smaller c^* when a transition is occurring from forward vortex sheet (FV_{sheet}) to 2P-reverse vortex sheet ($2P - RV_{\text{sheet}}$) behind the hydrofoil. At lower Re , Fig. 13(b) shows that the drag to thrust transition occurs at larger c^* , which reduces with increasing Re .

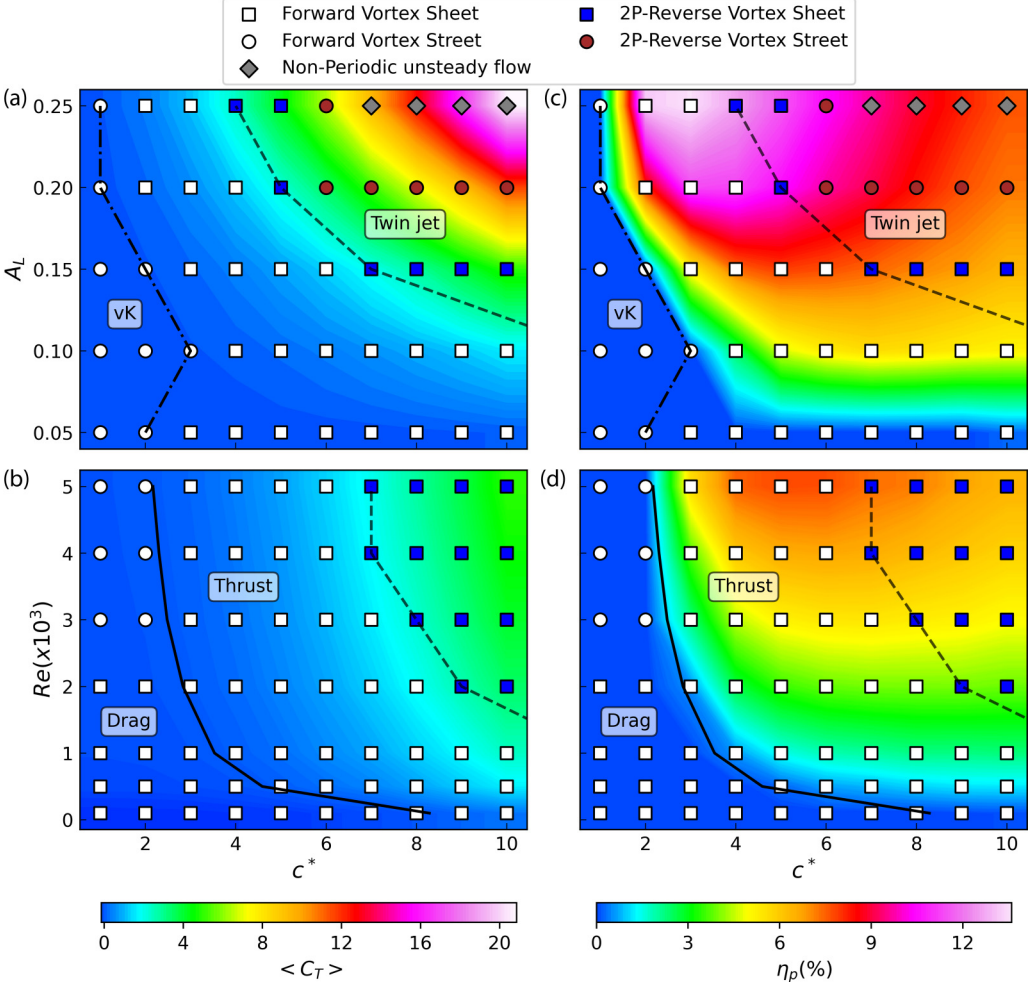


FIG. 13. Regime maps based on various modes of one-pair and two-pair (2P) forward/reverse vortex sheets/streets (F/R- $V_{\text{sheet/street}}$) behind the hydrofoil at (a), (b) $Re = 5000$ and (c), (d) $A_L = 0.15$. For various local amplitude-thickness ratio A_L , Re , and phase speed c^* , the maps are overlapped on contours of (a), (b) mean thrust coefficient $\langle C_T \rangle$, and (c), (d) propulsive efficiency η_p .

VII. SCALING ANALYSIS AND ITS COMPARISON WITH PRESENT RESULTS

Motivated by scaling analysis of thrust on a self-propelled hydrofoil by Gazzola *et al.* [55], we present the scaling of thrust force and propulsive efficiency for a hydrofoil with a traveling wave on its surface. We assume that the fluid is inviscid, incompressible, and irrotational. We ignore lift-based force in the scaling, considered in previous studies [15,56–59], since lift force is negligible for the present case of a traveling wave on the symmetrical hydrofoil.

Here, we only consider the added mass forces, similar to Gazzola *et al.* [55]. The mass of the fluid displaced by a single traveling wave between two peaks of a wave, as shown in Fig. 14, can be obtained as $m_f = \lambda a(x)$ in dimensional form. Thus, the total mass displaced by the traveling wave motion is

$$m_{f,\text{total}} \sim \lambda a(x) k \sim a(x). \quad (17)$$

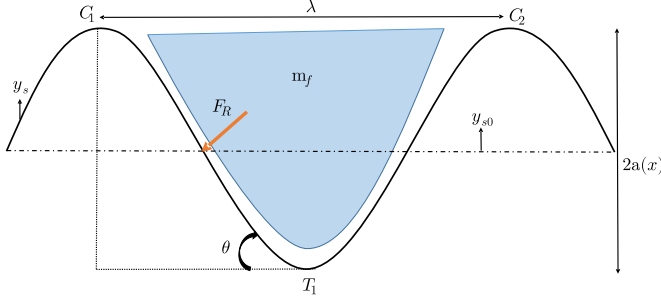


FIG. 14. A traveling wave with amplitude $a(x)$ and wavelength λ is shown. The reactive force by the fluid on the hydrofoil due to prescribed motion of traveling wave F_R is acting normal to the surface.

The acceleration on the mass of fluid-displaced scales with the acceleration of the surface generated by the traveling wave for an inviscid fluid and incompressible flow. Therefore, acceleration is obtained by differentiating Eq. (1) twice. Thus, the acceleration scales as

$$a_c \sim \frac{c^2 a(x)}{\lambda^2}. \quad (18)$$

The reaction force acting on the hydrofoil due to the displaced fluid (Fig. 14) scales as follows:

$$F_R = m_f a_c \sim \frac{c^2 a(x)^2}{\lambda^2}. \quad (19)$$

This force acts normal to the surface, and the thrust force on the hydrofoil due to the displaced mass of the fluid is $F_R \sin \theta$, where θ represents the local angle of the wave surface with the direction of the flow (Fig. 14). Here, we put $\sin \theta$ ($\approx \theta \sim a(x)/\lambda$) in Eq. (19), so the thrust force is given by

$$F_T = \frac{a(x)^3 c^2}{\lambda^3}. \quad (20)$$

Thus, the thrust coefficient can be written as

$$\langle C_T \rangle \sim K^3 c^{*2} A_L^3. \quad (21)$$

The power input P_{in} is calculated as the lift force multiplied by the hydrofoil velocity in y -direction V_s as shown in Eq. (10). The coefficient of power can be written as

$$C_P = F_R \cos \theta V_s, \quad (22)$$

where $F_R \cos \theta$ is the lift force and V_s is shown in Eq. (5). The velocity of hydrofoil scales as $V_s \sim K c^* A_L$. Therefore, the efficiency is expressed as follows:

$$\eta_p = \frac{\langle C_T \rangle}{C_P} = \frac{\tan \theta}{V_s} \sim \frac{1}{c^*}; \quad (23)$$

here $\tan \theta$ has been approximated as $A_m k$.

The variation of $\langle C_T \rangle$ with c^* is concurred with the scaling as shown in Fig. 8(a) as a quadratic variation of c^* with $\langle C_T \rangle$. Figure 15 shows the variation of $\langle C_T \rangle / c^{*2}$ [Eq. (21)] with different A_L . The black dashed line shows the cubic scaling for A_L in Fig. 15. As the value of K is constant for all the simulations plotted in Fig. 15, the plot shows the scaling of A_L with $\langle C_T \rangle / c^{*2}$. The cubic scaling agrees with the simulated results, as shown in Fig. 15. The $\langle C_T \rangle$ follows a cubic relation for all A_L . The results plotted in Fig. 15 are for the cases with $K = 10$ and $\text{Re} = 5000$. After reaching maximum, η_p declines inversely with c^* as shown in Figs. 8(a), 12(c), and 12(d).

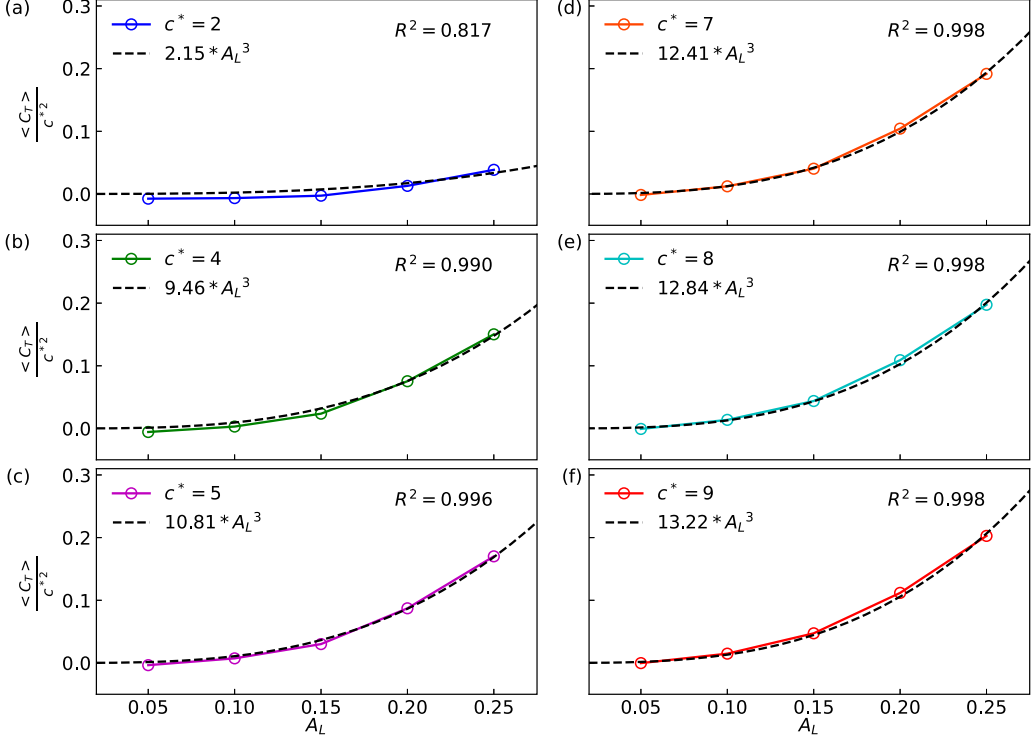


FIG. 15. Variation of $\langle C_T \rangle / c^{*2}$ with respect to A_L for different cases of c^* . The black dashed line shows the cubic proportion of A_L with C_T and the grey dashed dot line shows the square proportion. The results are for traveling wave with $K = 10$ at $Re = 5000$.

VIII. CONCLUSIONS

A LS-IIM-based in-house code is used for the present two-dimensional numerical study on free-stream flow across a NACA0012 hydrofoil with a traveling wave-based surface undulations. For a detailed nondimensional study at a constant wave number $K = 10$ and a phase difference of 180° between the top and bottom surface-undulations, the effect of local amplitude-thickness ratio A_L (0.05 to 0.25), phase speed c^* (1 to 10), and Reynolds number Re (100 to 5000) on the flow characteristics and propulsive performance are investigated. The conclusions drawn from the present paper are as follows:

(1) With increasing Re at low phase speed $c^* (\leq 2)$, the flow behind the hydrofoil undergoes a flow-transition from *steady* forward twin vortex *sheets* FV_{sheet} to *periodic* forward von Kármán vortex *street* FV_{street} ; similar to that for a flow across the stationary bluff body, whereas an opposite flow transition from FV_{street} to FV_{sheet} along with another transition from FV_{sheet} to 2P of reverse vortex sheet 2P-RV $_{sheet}$ are found with increasing c^* at $Re \geq 2000$. Although the flow behind the hydrofoil is almost steady in the FV_{sheet} regime, the surface undulation-induced unsteady flow is localized above and below the hydrofoil and loses its unsteadiness behind the hydrofoil.

(2) With increasing phase speed c^* at high $Re = 5000$, the flow transition from the periodic FV_{street} to steady FV_{sheet} is found at low amplitude-thickness ratio $A_L (\leq 0.1)$. At high A_L , we found many more flow transitions corresponding to FV_{sheet} to 2P-RV $_{sheet}$ at $A_L = 0.15$; also steady 2P-RV $_{sheet}$ to periodic 2P-RV $_{street}$ at $A_L = 0.2$ and 0.25.

(3) Pressure-suction mechanism is found as the mechanism for thrust generation due to surface-undulation, similar to that reported in the literature for whole-body undulations. However, the thrust generation is distributed over the pressure and suction side of each of the multiple waves ($K = 10$

here) in the surface undulations as compared to the thrust generated by a single wave in the body undulation. The spatial variation of the thrust shows that the first three wavy sections produce thrust for the half oscillation cycle while the other wavy sections contribute to the thrust in the next half-cycle. The variation of time-averaged thrust along the foil shows that the thrust is produced for all wavy sections except for the wavy section near the leading edge. However, the thrust contribution of the first wavy section for the first half-cycle is maximum. The time-averaged thrust is the maximum in the zones, where wave amplitude is the maximum.

(4) A threshold value of c^* , A_L , and Re exist to produce the thrust. Thrust increases monotonically with an increase in phase speed c^* , local amplitude-thickness ratio A_L , and Re . The viscous component of thrust decreases with c^* while the pressure component increases monotonically. The critical c^* at which surface undulation produces thrust decreases with increasing Re . Maximum propulsive efficiency is found in the forward vortex-sheet FV_{sheet} regime, which changes into a $2P-RV_{\text{sheet}}$ with increasing phase speed c^* .

(5) A scaling analysis was developed in this paper for surface undulation. For thrust coefficient C_T , the scaling is found as $C_T \sim K^3 c^{*2} A_L^3$. The propulsive efficiency η decays asymptotically as the inverse of c^* after reaching its maximum. In general, the numerical data is consistent with the proposed scaling laws.

The present paper elucidates the flow dynamics of traveling wave-based surface-undulations of a hydrofoil in a free-stream flow for higher local amplitude-thickness ratio A_L and Re for a wide range of c^* . However, the flow physics around very large $A_L = 0.25$ and large $c^* \geq 7$ requires further investigations to identify flow regimes corresponding to the nonperiodic unsteady flow. Also, effects of the phase difference ϕ_b and wave number K will be presented in our future work. The present results are potentially useful to design propulsion of autonomous naval vehicles.

ACKNOWLEDGMENT

We gratefully acknowledge financial support from the Naval Research Board, New Delhi, India (Grant No. NRB-403/HYD/17-18).

-
- [1] F. E. Fish and G. V. Lauder, Passive and active flow control by swimming fishes and mammals, *Annu. Rev. Fluid Mech.* **38**, 193 (2006).
 - [2] J. H. Arakeri and R. K. Shukla, A unified view of energetic efficiency in active drag reduction, thrust generation and self-propulsion through a loss coefficient with some applications, *J. Fluids Struct.* **41**, 22 (2013).
 - [3] F. Gosselin, E. De Langre, and B. A. Machado-Almeida, Drag reduction of flexible plates by reconfiguration, *J. Fluid Mech.* **650**, 319 (2010).
 - [4] R. Bhardwaj and R. Mittal, Benchmarking a coupled immersed-boundary-finite-element solver for large-scale flow-induced deformation, *AIAA J.* **50**, 1638 (2012).
 - [5] J. Wu, Y. L. Qiu, C. Shu, and N. Zhao, Flow control of a circular cylinder by using an attached flexible filament, *Phys. Fluids* **26**, 103601 (2014).
 - [6] A. Kundu, A. K. Soti, R. Bhardwaj, and M. C. Thompson, The response of an elastic splitter plate attached to a cylinder to laminar pulsatile flow, *J. Fluids Struct.* **68**, 423 (2017).
 - [7] E. Friedmann, J. Portl, and T. Richter, A study of shark skin and its drag reducing mechanism, in *Advances in Mathematical Fluid Mechanics* (Springer, Berlin, Heidelberg, 2009), pp. 271–285.
 - [8] S.-J. Lee and A.-T. Nguyen, Experimental investigation on wake behind a wavy cylinder having sinusoidal cross-sectional area variation, *Fluid Dyn. Res.* **39**, 292 (2007).
 - [9] A. Das, R. K. Shukla, and R. N. Govardhan, Existence of a sharp transition in the peak propulsive efficiency of a low- Re pitching foil, *J. Fluid Mech.* **800**, 307 (2016).

- [10] P. A. Dewey, B. M. Boschitsch, K. W. Moored, H. A. Stone, and A. J. Smits, Scaling laws for the thrust production of flexible pitching panels, *J. Fluid Mech.* **732**, 29 (2013).
- [11] S. A. Manjunathan and R. Bhardwaj, Thrust generation by pitching and heaving of an elastic plate at low Reynolds number, *Phys. Fluids* **32**, 073601 (2020).
- [12] M. J. David, R. N. Govardhan, and J. H. Arakeri, Thrust generation from pitching foils with flexible trailing edge flaps, *J. Fluid Mech.* **828**, 70 (2017).
- [13] G. C. Lewin and H. Haj-Hariri, Modelling thrust generation of a two-dimensional heaving airfoil in a viscous flow, *J. Fluid Mech.* **492**, 339 (2003).
- [14] Z. Wei and Z. C. Zheng, Mechanisms of wake deflection angle change behind a heaving airfoil, *J. Fluids Struct.* **48**, 1 (2014).
- [15] D. Floryan, T. Van Buren, C. W. Rowley, and A. J. Smits, Scaling the propulsive performance of heaving and pitching foils, *J. Fluid Mech.* **822**, 386 (2017).
- [16] A. Goza, D. Floryan, and C. Rowley, Connections between resonance and nonlinearity in swimming performance of a flexible heaving plate, *J. Fluid Mech.* **888**, A30 (2020).
- [17] J. Deng, X.-M. Shao, and A.-L. Ren, Numerical study on propulsive performance of fish-like swimming foils, *J. Hydrodyn.* **18**, 681 (2006).
- [18] N. Thekkethil, A. Sharma, and A. Agrawal, Unified hydrodynamics study for various types of fishes-like undulating rigid hydrofoil in a free stream flow, *Phys. Fluids* **30**, 077107 (2018).
- [19] A. Andersen, T. Bohr, T. Schnipper, and J. H. Walther, Wake structure and thrust generation of a flapping foil in two-dimensional flow, *J. Fluid Mech.* **812**, R4 (2017).
- [20] G. S. Triantafyllou, M. S. Triantafyllou, and M. A. Grosenbaugh, Optimal thrust development in oscillating foils with application to fish propulsion, *J. Fluids Struct.* **7**, 205 (1993).
- [21] L. Schouveiler, F. S. Hover, and M. S. Triantafyllou, Performance of flapping foil propulsion, *J. Fluids Struct.* **20**, 949 (2005).
- [22] R. Godoy-Diana, J.-L. Aider, and J. E. Wesfreid, Transitions in the wake of a flapping foil, *Phys. Rev. E* **77**, 016308 (2008).
- [23] T. Schnipper, A. Andersen, and T. Bohr, Vortex wakes of a flapping foil, *J. Fluid Mech.* **633**, 411 (2009).
- [24] S. Y. Shinde and J. H. Arakeri, Flexibility in flapping foil suppresses meandering of induced jet in absence of free stream, *J. Fluid Mech.* **757**, 231 (2014).
- [25] S. Y. Shinde and J. H. Arakeri, Physics of unsteady thrust and flow generation by a flexible surface flapping in the absence of a free stream, *Proc. R. Soc. London A* **474**, 20180519 (2018).
- [26] I. Borazjani and F. Sotiropoulos, Numerical investigation of the hydrodynamics of carangiform swimming in the transitional and inertial flow regimes, *J. Exp. Biol.* **211**, 1541 (2008).
- [27] G. V. Lauder, J. Lim, R. Shelton, C. Witt, E. Anderson, and J. L. Tangorra, Robotic models for studying undulatory locomotion in fishes, *Mar. Technol. Soc. J.* **45**, 41 (2011).
- [28] F. S. Essapian, *Speed-Induced Skin Folds in the Bottle-Nosed Porpoise *Tursiops Truncatus** (Museum of Comparative Zoology, Cambridge, USA, 1955).
- [29] G.-J. Dong and X.-Y. Lu, Characteristics of flow over traveling wavy foils in a side-by-side arrangement, *Phys. Fluids* **19**, 057107 (2007).
- [30] E. D. Tytell, The hydrodynamics of eel swimming II. Effect of swimming speed, *J. Exp. Biol.* **207**, 3265 (2004).
- [31] S. Taneda and Y. Tomonari, An experiment on the flow around a waving plate, *J. Phys. Soc. Jpn.* **36**, 1683 (1974).
- [32] B. D. Ivashchenko, K. P. Il'ichev, and S. N. Postolovskii, Hydrodynamic effect of a traveling wave, *Fluid Dyn.* **10**, 122 (1976).
- [33] A. M. Akbarzadeh and I. Borazjani, Reducing flow separation of an inclined plate via travelling waves, *J. Fluid Mech.* **880**, 831 (2019).
- [34] L. Shen, X. Zhang, D. K. P. Yue, and M. S. Triantafyllou, Turbulent flow over a flexible wall undergoing a streamwise travelling wave motion, *J. Fluid Mech.* **484**, 197 (2003).
- [35] F. Xu, W.-L. Chen, W.-F. Bai, Y.-Q. Xiao, and J.-P. Ou, Flow control of the wake vortex street of a circular cylinder by using a traveling wave wall at low Reynolds number, *Comput. Fluids* **145**, 52 (2017).

- [36] C.-J. Wu, L. Wang, and J.-Z. Wu, Suppression of the von Kármán vortex street behind a circular cylinder by a travelling wave generated by a flexible surface, *J. Fluid Mech.* **574**, 365 (2007).
- [37] G. Jones, M. Santer, and G. Papadakis, Control of low Reynolds number flow around an airfoil using periodic surface morphing: A numerical study, *J. Fluids Struct.* **76**, 95 (2018).
- [38] E. Thompson and A. Goza, Surface morphing for aerodynamic flows at low and stalled angles of attack, *Phys. Rev. Fluids* **7**, 024703 (2022).
- [39] P. Sooraj, A. Sharma, and A. Agrawal, Dynamics of co-rotating vortices in a flow around a bio-inspired corrugated airfoil, *Int. J. Heat Fluid Flow* **84**, 108603 (2020).
- [40] W. Chuijie, X. Yanqiong, and W. Jiezhi, fluid roller bearing effect and flow control, *Acta Mech. Sin.* **19**, 476 (2003).
- [41] A. M. Akbarzadeh and I. Borazjani, Controlling flow separation on a thick airfoil using backward traveling waves, *AIAA J.* **58**, 3799 (2020).
- [42] F.-B. Tian, X.-Y. Lu, and H. Luo, Propulsive performance of a body with a traveling-wave surface, *Phys. Rev. E* **86**, 016304 (2012).
- [43] F.-B. Tian, Y.-Q. Xu, X.-Y. Tang, and Y.-L. Deng, Study on a self-propelled fish swimming in viscous fluid by a finite element method, *J. Mech. Med. Biol.* **13**, 1340012 (2013).
- [44] L. J. Rosenberger, Pectoral fin locomotion in batoid fishes: Undulation versus oscillation, *J. Exp. Biol.* **204**, 379 (2001).
- [45] J. Lei, J. Zhang, and J. Niu, Effect of active oscillation of local surface on the performance of low Reynolds number airfoil, *Aerosp. Sci. Technol.* **99**, 105774 (2020).
- [46] A. Akbarzadeh, I. Borazjani, and U. Ogunka, The role of amplitude on controlling flow separation using traveling wave morphing, *AIAA Scitech* **2021** (2021).
- [47] N. Thekkethil and A. Sharma, Level set function–based immersed interface method and benchmark solutions for fluid flexible-structure interaction, *Int. J. Numer. Methods Fluids* **91**, 134 (2019).
- [48] N. Thekkethil and A. Sharma, *Hybrid Lagrangian-Eulerian method-based CFD development, application, and analysis, in Immersed Boundary Method* (Springer, Singapore, 2020), pp. 361–394.
- [49] J. Videler and F. Hess, Fast continuous swimming of two pelagic predators, saithe (*Pollachius virens*) and mackerel (*Scomber scombrus*): A kinematic analysis, *J. Exp. Biol.* **109**, 209 (1984).
- [50] C. Wardle, J. Videler, T. Arimoto, J. Franco, and P. He, The muscle twitch and the maximum swimming speed of giant bluefin tuna, *Thunnus thynnus* L., *J. Fish Biol.* **35**, 129 (1989).
- [51] P. W. Webb, Kinematics of lake sturgeon, *Acipenser fulvescens*, at cruising speeds, *Can. J. Zool.* **64**, 2137 (1986).
- [52] Md. M. Alam, Y. Zhou, H. X. Yang, H. Guo, and J. Mi, The ultra-low Reynolds number airfoil wake, *Exp. Fluids* **48**, 81 (2010).
- [53] N. Thekkethil, A. Sharma, and A. Agrawal, Three-dimensional biological hydrodynamics study on various types of batoid fishlike locomotion, *Phys. Rev. Fluids* **5**, 023101 (2020).
- [54] U. K. Müller, B. L. E. Van Den Heuvel, E. J. Stamhuis, and J. J. Videler, Fish foot prints: Morphology and energetics of the wake behind a continuously swimming mullet (*Chelon labrosus* risso), *J. Exp. Biol.* **200**, 2893 (1997).
- [55] M. Gazzola, M. Argentina, and L. Mahadevan, Scaling macroscopic aquatic locomotion, *Nat. Phys.* **10**, 758 (2014).
- [56] A. J. Smits, Undulatory and oscillatory swimming, *J. Fluid Mech.* **874**, P1 (2019).
- [57] T. Liu, S. Wang, X. Zhang, and G. He, Unsteady thin-airfoil theory revisited: Application of a simple lift formula, *AIAA J.* **53**, 1492 (2015).
- [58] K. W. Moored and D. B. Quinn, Inviscid scaling laws of a self-propelled pitching airfoil, *AIAA J.* **57**, 3686 (2019).
- [59] I. E. Garrick, Propulsion of a flapping and oscillating aerofoil, NACA technical report, 1936.